

Explaining the non-intuitive surface self-assembly of acenequinones on Ag(111): More than just LEGO

A. Jeindl¹, J. Domke², L. Hörmann¹, F. Sojka², R. Forker², T. Fritz², and O.T. Hofmann^{1*}

¹ Institute of Solid State Physics, NAWI Graz, Graz University of Technology, Petersgasse 16, 8010 Graz, Austria

² Institute for Solid State Physics, Friedrich Schiller University Jena, Helmholtzweg 5, 07743 Jena, Germany

*Corresponding author: o.hofmann@tugraz.at

Abstract

The rapid development of nanotechnology requires optimizing materials and material combinations at a molecular level. A common tool is to exploit chemical intuition and equip molecules with functional groups to obtain specific molecular arrangements. However, whether functionalization yields the expected results depends sensitively on the parent molecules. Our experimental investigations show that despite chemical similarity, profoundly different structures occur for the prototypical system of acenequinones on Ag(111). To understand this behavior from first principles, we perform in-depth investigations with machine-learning-assisted quantum mechanical modeling. This allows us to understand the monolayer motifs and gain insight into the interaction mechanisms at play. We attribute the different structures to a non-intuitive molecule-size-dependent tradeoff between adsorbate-substrate interactions governing molecular orientations, adsorbate-adsorbate interactions favoring close-packing, and steric hindrance partly inhibiting otherwise beneficial structures. This demonstrates that for the prediction of surface structures an in-depth understanding about the specific interactions, beyond chemical intuition, is vital.

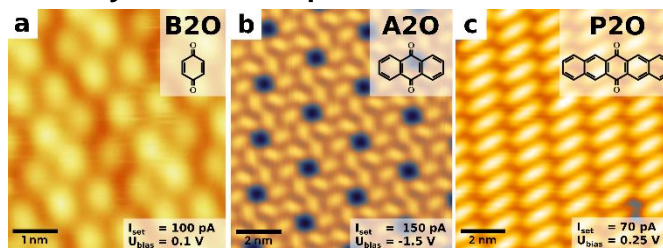
Main

Many properties of thin films, such as optical properties¹ or electrical conductivity,² are determined by the structure they assume upon adsorption on the substrate.³ To engineer functional interfaces, it is therefore imperative to understand and predict which structures form for a given material combination.^{4,5} At a single molecule level, relevant handles to influence their properties are well known. A typical example are conjugated organic molecules, which are relevant for organic nanoelectronics.^{6–8} There, increasing the π -electron backbone or introducing functional groups systematically affects optical properties.^{9–12} Changing either the backbone or functional groups will also change the molecule's crystal polymorphs and its physical properties^{13–16} in non-obvious ways. Particularly for thin films and even more so for monolayers, the complex interplay between intermolecular and molecule-surface interactions can lead to the formation of new packing motifs.³ Several groups design molecules based on chemical intuition to endow them with specific, dominant interactions (e.g., long-range repulsion,^{17,18} non-covalent interactions,^{19–24} or steric blocking²⁵). In previous experiments, this resulted in the formation of intricate motifs where the driving forces leading to self-assembly could then, in hindsight, be analyzed by experimental and theoretical methods.^{4,5,25–27,17–24} However, with a few exceptions,²² a holistic design of particular motifs is still prevented by the fact that the driving forces for self-

assembly cannot be easily transferred from one case to another. Quite contrary, even systems that have similar interactions can form disparate structures.

Here, we exemplify this via a homologous series of molecules with identical functionalization, namely the acenequinones 1,4-benzoquinone (B2O), 9,10-anthraquinone (A2O), and 6,13-pentacenequinone (P2O). In all three molecules, the functional groups provide directed forces for self-assembly via (i) highly attractive intermolecular interactions between the oxygens and hydrogens, and (ii) a strong molecule-substrate interaction due to surface-induced aromatic stabilization.²⁸ Conversely, the backbone interacts non-site-specific via van-der-Waals forces. When depositing up to a single monolayer on Ag(111), we find three entirely different structures (Fig. 1; a detailed characterization is given later in this work). While the smallest molecule, B2O, exhibits a simple 2D surface pattern, the larger A2O forms symmetric hexagonal rings with voids in between. The largest molecule of this series, P2O, crystallizes in close-packed molecular rows, as also found by others.^{28,29} Despite the chemical similarity, the backbone size thus decisively determines which motifs form.

Fig. 1: Experimental STM images for molecular monolayers of acenequinones



Constant-current scanning tunneling microscopy (STM) images for **a**, benzoquinone (B2O) **b**, anthraquinone (A2O) and **c**, pentacenequinone (P2O) on a Ag(111) surface prepared by physical vapor deposition.

We provide systematic insight into how the backbone size affects the driving forces leading to the formation of these motifs. To this end we predict, based on first principles, which on-surface motifs the three acenequinones form on Ag(111), utilizing a combination of density functional theory (DFT) and machine learning (details see Methodology). First, we focus on the interactions of individual molecules with the Ag(111) surface to unveil trends in the molecule-substrate interaction. We then investigate the intermolecular interactions of close-packed molecular layers on the Ag surface. Mapping the intermolecular energies onto specific molecule parts enables us to identify the main contributors for polymorph formation. This procedure allows extracting general trends for those interactions. Most importantly, we find that the aspect ratio of the molecules plays a large (and hitherto probably undervalued) role, determining how many favorable interactions with neighboring adsorbates a single molecule can obtain.

Results and discussion

The interaction of individual molecules with Ag(111)

Individual acenequinone molecules interact with the Ag(111) surface by site-specific interactions between the oxygens and the metal, as well as non-site-specific van-der-Waals interactions between backbone and substrate. One could thus expect that in the absence of intermolecular interactions all molecules prefer the same or similar adsorption geometries on the metal (defined by the adsorption site on the primitive metal substrate and azimuthal rotation of the molecule). Testing this hypothesis and finding all local minima for the molecules on the surface would, in principle, require an exhaustive global structure search. This is infeasible even for the most advanced algorithms^{30,31} due to the high configurational complexity.³² Thus, we performed a two-step procedure that starts with pre-screening of a potential energy surface (PES) with reduced dimensionality, followed by full geometry optimizations, where the whole molecule as well as the two topmost metal layers were allowed to relax (details in Supplementary Section 1.3).

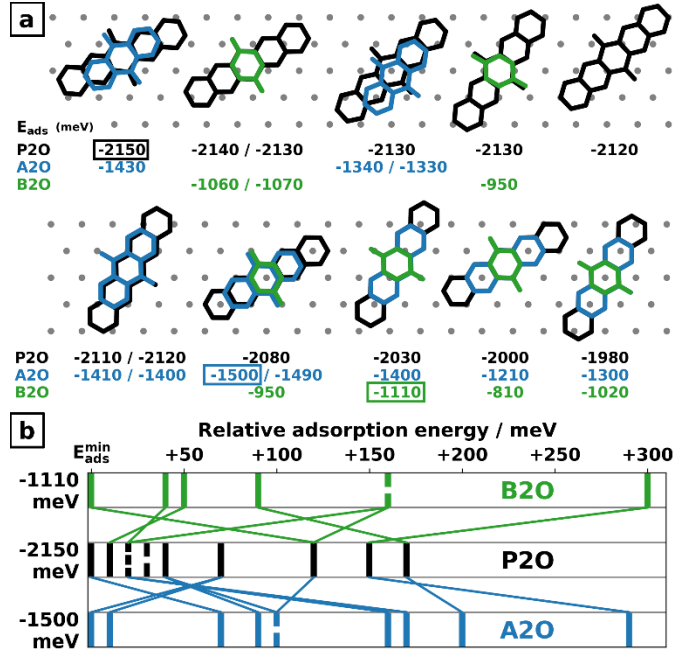
To analyze the results, we focus on three important aspects (Fig. 2): (i) the adsorption geometries, (ii) the adsorption energies, and (iii) their energy distribution (i.e., how many adsorption geometries exist within a certain energy range). Despite different backbone lengths, the adsorption geometries are rather similar. For all adsorption geometries of B2O and A2O we find a corresponding adsorption geometry of P2O, where the oxygens are approximately in the same positions. Fig. 2a illustrates this point, showing the P2O geometries sorted by their adsorption energy and overlaying the corresponding B2O and A2O geometries.

Although the adsorption geometries are very similar for the three molecules, their energetic ranking is very different (Fig. 2b). This suggests a key-lock-like interaction between the acenequinones and the surface. Presumably, which geometries are stable is governed (mostly) by the oxygens that bind to specific sites on the Ag(111) surface. Conversely, their energetic ranking depends on the registry of the backbone with the surface. For the most stable geometries, the adsorption energy increases with increasing backbone size (-1.11 eV for B2O, -1.50 eV for A2O, -2.15 eV for P2O), as expected. In passing, we note that the observed non-additivity of adsorption energies with respect to molecule size (additional aromatic rings) is at first surprising, but has also been observed for acenes on Au(111).³³

As introduced above, the second factor determining which motif forms is the intermolecular interaction. An energetically unfavorable adsorption geometry might also be part of the energetically most favorable motif if it accommodates more attractive intermolecular interactions compensating the loss in adsorption energy.

For our systems, the range of adsorption energies decreases with increasing molecule size from 300 meV for B2O to 170 meV for P2O. Concomitantly, an increasing number of stable adsorption geometries is found energetically close to the most stable geometry, making more adsorption geometries easily accessible for monolayer formation. Especially for P2O, already 8 of its 12 adsorption geometries are found within a range of 50 meV. In general, making the molecule larger by adding benzene rings to the quinone backbone increases the number of adsorption geometries and increases adsorption energies. Simultaneously, the energy difference between different minima decreases, leading to a weaker adsorption-geometry dependence. This is a direct consequence of the inherent incommensurability of the acene backbone with the Ag(111) surface: the larger the backbone, the more the energetic landscape of the molecule-substrate potential becomes smoothed out.

Fig. 2: Analysis of the adsorption geometries and energies



a, Visualization of all symmetry-inequivalent adsorption geometries for B2O, A2O and P2O molecules with their corresponding adsorption energies (negative values of E_{ads} denote energy gain upon adsorption). Surface substrate atom positions are indicated with grey dots. Boxes mark the energetically best adsorption geometries. Two energies for a single visualized geometry mark hcp- and fcc-hollow sites, respectively (i.e., there are two adsorption geometries which only differ due to symmetries of the second substrate layer). There, the left energy corresponds to the geometry shown here (hcp hollow).

b, Spread of all adsorption geometry energies for all three molecules relative to the energy of the respective best geometry. Adsorption energies with multiple energetically equivalent geometries are indicated with dashed lines. There, the number of dashes is equal to the number of geometries. The colored connecting lines indicate the energetic reordering compared to the P2O geometries.

Intermolecular interactions on the surface

Now that we understand interactions of individual molecules with the surface, we proceed to the intermolecular interactions on the surface. The number of possible arrangements of molecules on the surface, however, is enormous.³² This makes an exhaustive mapping of the interactions intractable. A similar challenge is encountered for first-principle structure determination, where interactions are approximated using intermolecular interactions from gas phase data³⁴ or via modified force fields.³⁵ Those methods perform best for low coverages or weak molecule-surface interaction. Here, however, the focus is on close-packed structures

with strong molecule-surface interactions, rendering those methods inapplicable.

For this reason, we used the SAMPLE³⁶ approach. It uses the previously mentioned adsorption geometries as constituents to build a large but discrete set of potential motifs with (here) up to six molecules per unit cell and various unit cell sizes (details in Methodology). From the millions of potential motifs, we selected the approx. 250 most diverse candidates using D-optimality³⁷ and calculated their formation energies using DFT. These calculations were then used to infer all relevant molecule-substrate and intermolecular interactions on the surface using the energy model (equation 2) combined with Bayesian linear regression.

$$E = \sum_{geoms} N_g U_g + \sum_{pairs} N_p V_p \quad (2)$$

Here, U_g is the adsorption energy of a molecule with the adsorption geometry g , and V_p is the interaction between every pair of molecules (called “pairwise interaction” hereafter) in the motif. N_g and N_p denote how often the corresponding interactions appear in each motif. With this method we can predict the formation energies for all potential motifs with a leave-one-out cross validation error of less than 20 meV per adsorbate molecule. Fig. 3a gives an overview over the intermolecular interaction energies (V_p) for the three investigated systems. The most attractive interactions lead to an energy gain of up to 200 meV for a pair of B2O molecules, 250 meV for A2O and 300 meV for P2O. Hence, for larger molecules also the intermolecular interactions become stronger.

Besides the total interaction energies within the motifs, the specific form of the energy model also allows to extract and visualize all pairwise interactions used in the model. Fig. 3b shows these interactions spatially resolved for B2O, A2O and P2O. There, the molecule in the center is kept fixed and the second molecule is moved (at fixed rotation) to all different possible adsorption sites around it. Each circle indicates the center of the second molecule with the color of the circle corresponding to the interaction energy of this molecular pair. The discretization of the pairwise interactions stems from the usage of adsorption geometries as fixed building blocks. The general form of interactions is similar for all three systems and independent of the size of the backbone.

For a deeper insight, we investigate the influence of the molecular fragments by breaking up V_p into a sum of fragments V_p^f :

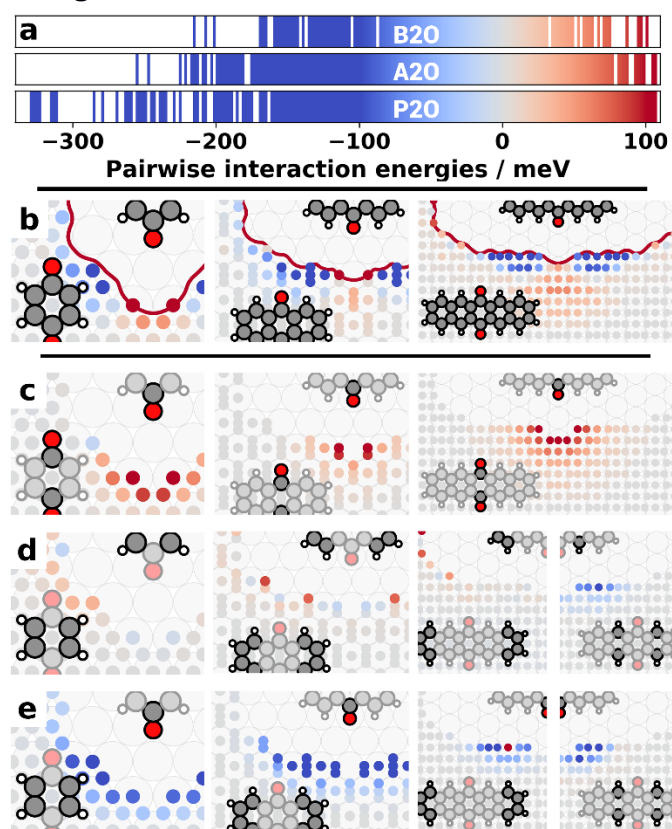
$$E = \sum_{geoms} N_g U_g + \sum_{pairs} \sum_{fragments} N_p^f V_p^f \quad (3)$$

This allows us to map intermolecular interactions onto specific parts. Fig. 3c-e show the interactions between oxygens (c), between carbon rings (d), and the interactions between oxygens and rings (e).

The intermolecular oxygen interactions (Fig. 3c) are almost exclusively repulsive, following Coulomb-like behavior due to the partially negatively charged oxygen atoms on both molecules. Interactions between rings (Fig. 3d) are dominated by the proximity of hydrogen atoms. They are slightly repulsive for B2O and slightly attractive for the larger molecules, but the energy range of these interactions is mostly within the model uncertainty. The most attractive interactions occur between carbon rings and oxygens (Fig. 3e). For P2O the discrimination of these contributions between inner and outer carbon rings shows that the main attraction stems from the outermost carbon rings. While those results are qualitatively consistent with chemical intuition, we

resolve the interactions based on chemical groups in a quantitative and position-specific way, revealing the general intermolecular interaction characteristics for a homologous series of acenequinones.

Fig. 3: Visualization of pairwise intermolecular energies and their contributions



a, Distribution of interaction energies for the three molecules under investigation. Colored areas represent interactions present in the given energy window;

b, Total pairwise interaction energies for all three molecules. Each circle represents a possible pairwise interaction between the central molecule and another molecule centered at the circle position. The red contour shows the minimal distance before a pair is considered colliding. The circle color indicates the corresponding interaction energy (same color scale as in **a**);

c-e, pairwise interaction energies mapped onto different molecule parts: **c**, oxygen - oxygen **d**, hydrogen - hydrogen **e**, oxygen - hydrogen interactions

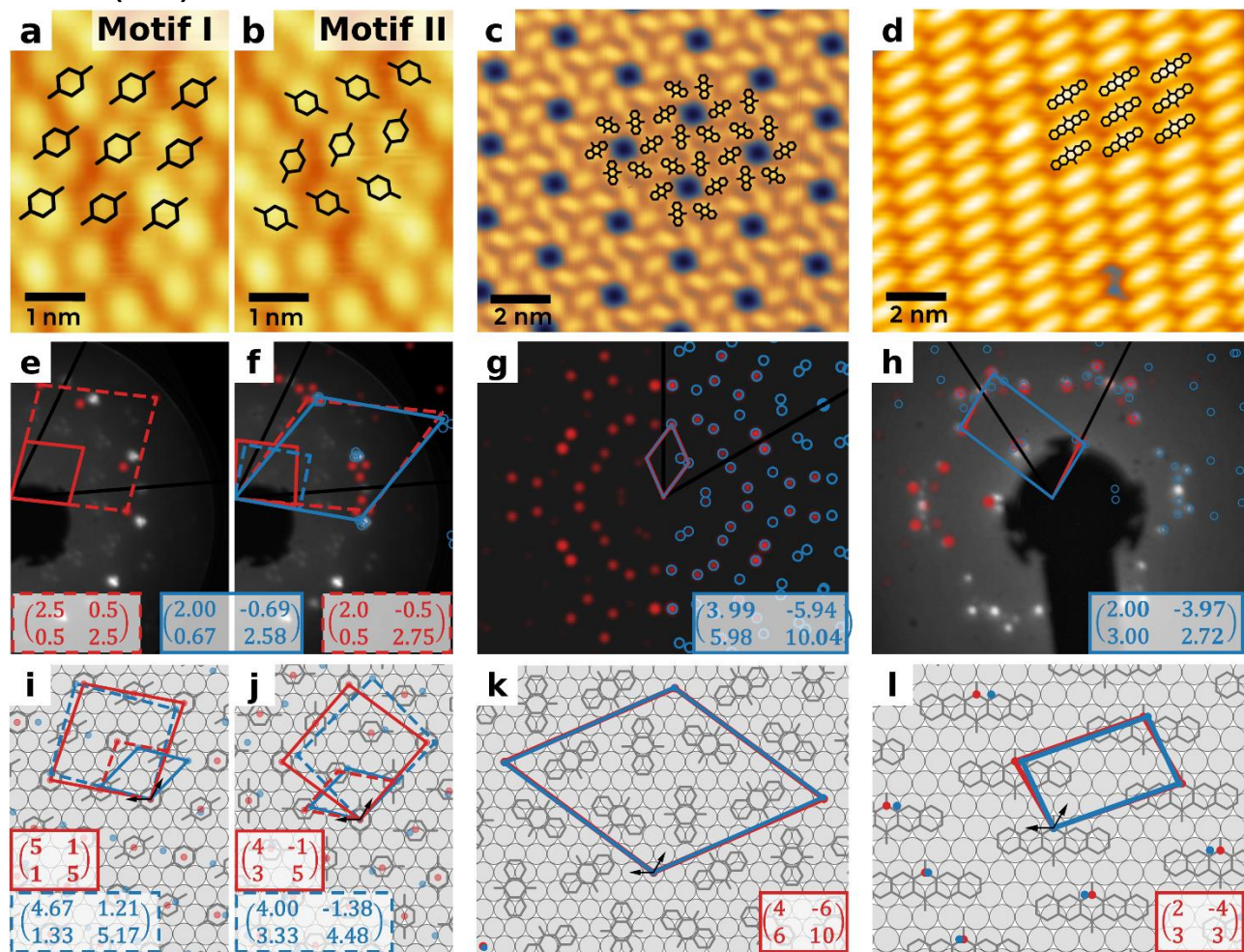
Stable motifs in theory and experiment

Having characterized all relevant interactions on the surface, we can now evaluate which motifs are expected to be observed. For this, we evaluated the energy model (equation (2)) for all the millions of candidates and identified the best motifs in terms of formation energy per molecule. The details of the prediction process are given in Supplementary Section 3. In the following, we focus on the structures predicted to be energetically most favorable and their comparison to the experimental thin films prepared via physical vapor deposition in ultra-high vacuum (details in Supplementary Section 2.1). We note that the phases shown in Fig. 1 (and

discussed here in more detail) are not the only structures that form upon deposition. A detailed description of the full polymorphism is beyond the scope of this manuscript and will be provided elsewhere.

The qualitative agreement between theory and experiment can already be seen in Fig. 4a-d. To obtain a quantitative insight, we compare both, the experimental low energy electron diffraction (LEED) images and diffraction patterns obtained via fast Fourier transformation (FFT) of the scanning tunneling microscopy (STM) images (details in Supplementary Section 2.2), with kinematic scattering simulations for the predicted structures, taking into account the tabulated structure factors for all atoms (see Supplementary Section 1.5). Fig. 4e-h compares the experimental diffraction patterns and deduced unit cells for B2O, A2O and P2O to our best-fitting low-energy predictions.

Fig. 4: Comparison of theoretical findings (red) with experimental results and interpretations thereof (blue)



a-d, Comparison of STM experiments (see Fig. 1) with theoretically predicted surface polymorphs. **e-h,** Comparison of theoretical LEED patterns obtained via kinematic diffraction theory (red) to fits of FFTs from STM images (blue) and LEED images; primary electron energies are 27 eV for B2O and 48 eV for P2O. **i-l,** Visualization of the real-space on-surface arrangement. The epitaxy matrices represent the unit cells in the respective substrate basis given by the black arrows. Fit uncertainties for the experimental epitaxy matrices (blue) are below 0.08 for all elements (details in Supplementary Table 2). For B2O, two possible theoretical phases are shown. While LEED experiments reveal the primitive adsorbate unit cell, simulations for B2O require 4 molecules in a commensurate supercell. The dashed unit cells in (**e-f**) and (**i-j**) therefore represent transformed cells to obtain comparability (experimental cells replicated; simulated cells reduced).

P2O exhibits multiple different motif candidates within the prediction uncertainty. All of them contain the same molecular rows observed in experiment. However, our model allows for various relative arrangements of these rows (see Supplementary Fig. 7). The best structure with parallel rows contains a single molecule per unit cell and an area of $125.9 \text{ \AA}^2/\text{molecule}$. It is in excellent agreement with the experimentally deduced structure, not only within the STM image (Fig 4d) but also with respect to spot positions and intensities (Fig. 4h). The lattice lengths agree perfectly for the long and within 4 % for the short axis. The enclosed angle agrees within 5° (Table 1).

The experimental preparation of A2O led to well-ordered structures exhibiting a periodic hexagonal pattern. As can be seen in the STM image (Fig. 4c) the experimental surface structure is in good agreement with the energetically most favorable theoretical structure containing six molecules per unit cell with an area of $88.6 \text{ \AA}^2/\text{molecule}$. This cell shows excellent agreement with the predicted structure within fit uncertainties (Fig. 4g).

Table 1: Comparison of experimental (grey background) and theoretical unit cells.

a_1 , a_2 : Lengths of lattice vectors derived from the epitaxy matrices in combination with the theoretical substrate lattice vectors (primitive lattice constant 2.842 \AA); Γ : Angle between lattice vectors; θ : Angle between first lattice vector and primitive substrate axis; A: Unit cell area.

	$a_1 [\text{\AA}]$	$a_2 [\text{\AA}]$	$\Gamma [^\circ]$	$\theta [^\circ]$	A [\AA^2]
B2O*	13.8	11.4	88.5	-14.3	157.4
	13.0	12.4	94.3	-10.9	160.9
A2O	24.6	24.9	120.0	-36.5	530.0
	24.8	24.8	120.0	-36.6	531.6
P2O	15.0	8.2	95.9	40.8	121.3
	15.0	8.5	100.9	40.9	125.9

*Data for Motif II, for other unit cells see Supplementary Table 2

For B2O, we predict the energetically best motif (labeled Motif I) to contain two non-equivalent molecules per primitive unit cell. The molecules in this cell are oriented in parallel but located at different adsorption sites, i.e., they are (slightly) non-equivalent. Within SAMPLE, we also find energetically low-lying defects where rows of molecules are rotated by 90° , which costs 100 meV per defect while allowing for a denser packing of the B2O molecules. For the sake of discussion, we also consider a limiting case where every other row consists of these defects. This structure (Fig. 4j), which will be called Motif II hereafter, contains four non-equivalent molecules. For comparability we also use an equivalent cell with four molecules for Motif I (Fig. 4i).

The interpretation of the experimental diffraction pattern (shown in blue in Fig. 4f, details explained in Supplementary Section 2.2) indicates that B2O exhibits a line-on-line³⁸ registry. Converting that periodicity

into real space (Fig. 4j) shows that the computed and experimental lattice vectors differ only by -6 % and +8 %, respectively, while the unit cell areas differ only by 2 %. The enclosed angle is reproduced within 6°. We attribute these minor variations to the fact that the calculations require periodic boundary conditions which artificially and unavoidably enforce commensurability between the adsorbate and the substrate, which is different from the line-on-line registry in the real motif.

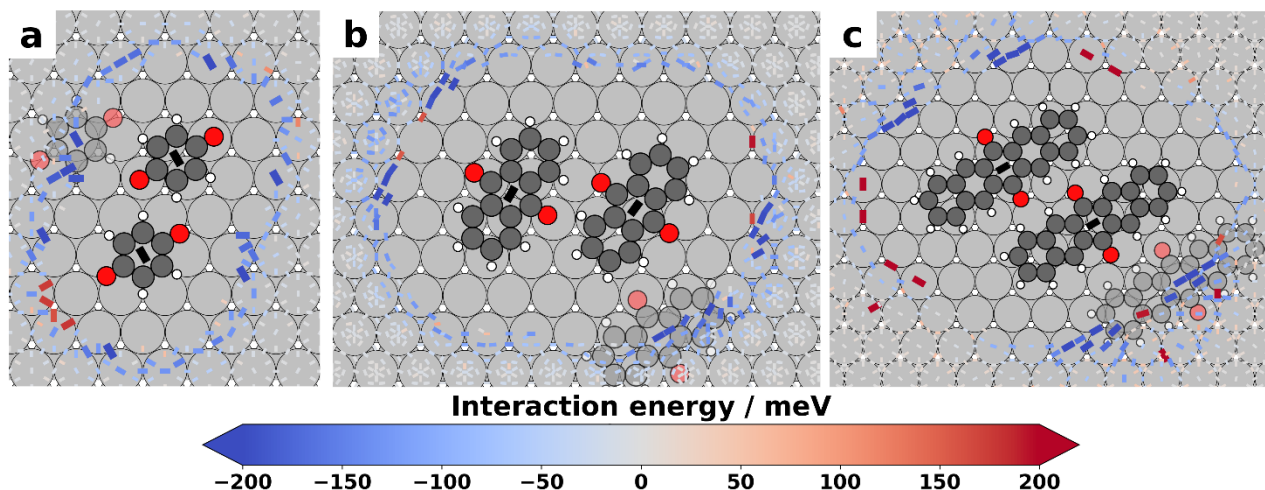
A summary of the numerical values for the discussed cells is presented in Table 1. More details for all cells shown in Fig. 4 are given in Supplementary Table 2. The agreement between our first-principles structure search and the experimentally found motifs underlines the fidelity of our analysis.

The last ingredient: steric hindrance

We have shown earlier in this work that the pairwise interactions as well as the molecule-surface interactions are similar for all three different systems. Nevertheless, the motifs observed experimentally and predicted theoretically exhibit substantially different features. This shows that there must be a crucial, hitherto missing, factor influencing the packing motifs formed.

This factor is the steric hindrance between molecules (Fig. 5). To illustrate and quantify this effect, we took the energetically most favorable pair for each system and evaluated the interactions with a third molecule at different orientations and positions. The resulting visualization is similar to Fig. 3b, but now the orientation of the outer molecule is visualized via the orientation of a rectangle. All rectangles were scaled according to their absolute energy to focus on stronger interactions.

Fig. 5: Steric hindrance visualized via trimer interactions



Trimer interactions visualizing all possible interactions of the energetically best pair with an outer molecule for (a) B2O, (b) A2O and (c) P2O. Each rectangle represents a molecule centered at the rectangle's midpoint, with its backbone orientation indicated by the long axis of said rectangle. The respective rotation indicates the energetically most favorable third molecule at this specific point, all other rotations at each site were discarded for clarity. The rectangles are scaled according to their absolute energy value to highlight strong interactions. The third, semi-transparent molecule indicates an energetically favorable geometry.

This visualization reveals that B2O can arrange such that the energetically most favorable interactions in all directions can be exploited for monolayer formation, leading to highly attractive interactions in four directions

for each molecule. A2O can build structures with molecular triangles, which allow three highly attractive interactions per molecule, as can be seen on the lower right corner of Fig. 5b. For P2O, the conjugated backbone is so long that the attractive hydrogen-oxygen interactions can only be formed with two neighbors. This makes interactions involving molecules rotated relative to each other energetically much less favorable, leading instead to long rows of molecules aligned parallel to each other.

Conclusions

In this work, we addressed the question why – in salient contrast to intuition – molecules with identical functionalization form completely different structural motifs on a metal surface, and whether insights and general trends for the on-surface self-assembly mechanisms can be retrieved from first principles without prior experimental input. To understand this behavior and reveal general trends, we investigated all the interaction mechanisms involved.

For individual molecules on the surface, the increasing molecule size increases the number of local minima while decreasing the energetic corrugation. Nonetheless, the adsorption geometries that occur for all molecules, are similar. The main intermolecular interactions driving the motif formation in acenequinones are a balance of attractive interactions between oxygens and hydrogen atoms counteracted by repulsive oxygen-oxygen interactions. The relative strengths of these interactions differ between the three investigated molecules, but not sufficiently to explain the vastly different surface structures. The more varying driving force is steric hindrance: The compact structure of B2O allows four oxygen-hydrogen interactions per molecule. These interactions lead to a brick-wall structure. For A2O, the larger backbone only accommodates three of these interactions. Hence, triangular building blocks form, which lead to the observed hexagonal ring-like motif. The even larger P2O molecules can only interact favorably with two neighboring molecules. The anisotropy of these interactions leads consequentially to the parallel alignment of P2O, thereby forming molecular rows. Our findings are backed by a remarkable agreement between theoretically predicted structures and experimentally resolved packing motifs.

These insights showcase that the vastly different surface patterns are driven by a changing balance of surface-molecule and intermolecular interactions in combination with steric hindrance upon increasing the molecule size. Even for relatively simple systems like acenequinones it is therefore challenging, if not outright impossible, to predict or engineer the monolayer structures based on chemical intuition alone. On a more positive note, advanced computational tools based on machine-learning, such as our SAMPLE³⁶ approach, allow to retrieve quantitative interaction energies and extract general trends for the interaction mechanisms. With enough structures investigated, we expect this to pave the way for a more holistic design of surface structures.

Methodology

All calculations were performed with the FHI-aims package³⁹ using the exchange-correlation functional PBE.⁴⁰ Long-range dispersion was included via the TS^{surf} correction.^{41,42} The integration in k-space was performed with a Gamma-centered grid with a well converged density of 36 points per primitive lattice direction and one k-point in z direction. As our calculations involved unit cells with different shapes, the k-points were scaled according to the length of the unit cell vectors. The periodic nature of our systems allowed us to use the repeated slab approach with a unit cell height of 80 Å (including >50 Å of vacuum), a dipole correction,⁴³ and eight layers of Ag with a mixed-quality numerical basis set (details in Supplementary Section 1.1). With this approach, all adsorption energies were converged to a methodological uncertainty below 20 meV per adsorbate molecule.

The adsorption geometries were found by first optimizing a single molecule on the surface and consecutively utilizing the BOSS approach³¹ to find all local extrema in the three-dimensional (x, y, and rotation around molecular axis) PES. Subsequently, geometry optimizations for the full molecule and substrate were performed from all extrema in the aforementioned PES. All final adsorption geometries, where at least one atom position differed by more than 0.1 Å (with symmetries taken into account), were considered as separate adsorption geometries. We define the adsorption energy as $E_{ads} = E_{sys} - E_{sub} - E_{mol}$ where E_{sys} is the energy of the combined system, E_{mol} the energy of a molecule in the gas phase, and E_{sub} the energy of the pristine Ag slab with the two upper layers pre-relaxed. Negative values of E_{ads} denote energy gain upon adsorption.

The SAMPLE³⁶ approach takes the surface atom positions in a given unit cells as a discrete grid and generates all combinations of building blocks at all possible positions within the unit cell and then removes colliding structures. As building blocks, it uses all adsorption geometries with all their symmetry equivalents on the respective metal surface. To not only be limited to a single unit cell, with SAMPLE we also generate an exhaustive set of unit cells for a given unit cell size (number of substrate atoms). For all three molecules in this study we varied the unit cell sizes and number of molecules per cell to ensure that experimentally feasible configurations are part of the prediction set (details in Supplementary Section 1.4). The training set for the SAMPLE approach was chosen with experimental design employing the D-optimality criterion³⁷ on interactions in the configurations. For the description of the different configurations within SAMPLE, the species dependent feature vector, considering distances between hydrogens and oxygens in all combinations, was used. All hyper parameters were thoroughly converged to robust values (Supplementary Section 1.2). To further reduce the computational costs, we first calculated the training configurations as free-standing monolayers (i.e., removed the metal substrate) and used the resulting fit parameters for the pairwise interaction energies as priors for the on-surface systems. With this methodology we could reduce the number of needed training calculations to 249 for B2O, 245 for A2O and 84 for P2O.

The organic molecules (B2O, A2O and P2O) were obtained as powders from Sigma-Aldrich, purified via sublimation prior to use, and deposited at room temperature (296 K) via physical vapor deposition on Ag(111) single crystals (cleaned by repeated Ar⁺ sputtering at 700 eV) in an ultra-high vacuum chamber (base pressure < 5·10⁻¹⁰ mbar). For details see the Supplementary Section 2.1. After deposition, the P2O samples were additionally gently heated while being monitored by LEED until a well-ordered structure became visible. For

the quantitative structural analysis, the samples were first characterized by distortion-corrected LEED⁴⁴ at room temperature including a numerical fitting of the assumed surface unit cell in reciprocal space to the measured LEED pattern (LEEDLab 2018 version 1.4). After LEED examinations, the samples were transferred into a low-temperature scanning tunnelling microscope (SPECS JT-LT-STM/AFM with Kolibri Sensors) and measured in constant-current mode at 4.5 K for A2O and 1.2 K for B2O and P2O. Afterwards, the obtained STM images were subjected to a two-dimensional Fourier transform and the epitaxy matrices were determined from those, utilizing the same software tools that were used for the LEED measurements, as already described elsewhere.^{45–47}

Data availability

The theoretical calculations used in this manuscript are available via the NOMAD database as separate data sets authored by Andreas Jeindl. DOIs to the sets will be provided prior to publication. Experimental details are provided in the Supplementary Information; further experimental data is available upon request.

Code availability

The SAMPLE code is freely available and can be downloaded at www.if.tugraz.at/hofmann

References

1. Forker, R., Gruenewald, M. & Fritz, T. Optical differential reflectance spectroscopy on thin molecular films. *Annu. Reports Prog. Chem. - Sect. C* **108**, 34–68 (2012).
2. Zhang, Y. *et al.* Probing Carrier Transport and Structure-Property Relationship of Highly Ordered Organic Semiconductors at the Two-Dimensional Limit. *Phys. Rev. Lett.* **116**, 016602 (2016).
3. Jones, A. O. F., Chattopadhyay, B., Geerts, Y. H. & Resel, R. Substrate-induced and thin-film phases: Polymorphism of organic materials on surfaces. *Adv. Funct. Mater.* **26**, 2233–2255 (2016).
4. Barth, J. V., Costantini, G. & Kern, K. Engineering atomic and molecular nanostructures at surfaces. *Nature* **437**, 671–679 (2005).
5. Bartels, L. Tailoring molecular layers at metal surfaces. *Nat. Chem.* **2**, 87–95 (2010).
6. Witte, G. & Wöll, C. Growth of aromatic molecules on solid substrates for applications in organic electronics. *J. Mater. Res.* **19**, 1889–1916 (2004).
7. Ye, Q. & Chi, C. Recent highlights and perspectives on acene based molecules and materials. *Chem. Mater.* **26**, 4046–4056 (2014).
8. Anthony, J. E. Functionalized acenes and heteroacenes for organic electronics. *Chem. Rev.* **106**, 5028–5048 (2006).
9. Gierschner, J., Cornil, J. & Egelhaaf, H.-J. Optical Bandgaps of π -Conjugated Organic Materials at the Polymer Limit: Experiment and Theory. *Adv. Mater.* **19**, 173–191 (2007).
10. Rieger, R. & Müllen, K. Forever young: Polycyclic aromatic hydrocarbons as model cases for structural and optical studies. *J. Phys. Org. Chem.* **23**, 315–325 (2010).
11. Kaur, I. *et al.* Substituent effects in pentacenes: Gaining control over HOMO-LUMO gaps and photooxidative resistances. *J. Am. Chem. Soc.* **130**, 16274–16286 (2008).

12. DiLabio, G. A., Pratt, D. A. & Wright, J. S. Theoretical calculation of ionization potentials for disubstituted benzenes: Additivity vs non-additivity of substituent effects. *J. Org. Chem.* **65**, 2195–2203 (2000).
13. Desiraju, G. R. Crystal engineering: From molecule to crystal. *J. Am. Chem. Soc.* **135**, 9952–9967 (2013).
14. Robb, M. J., Ku, S.-Y., Brunetti, F. G. & Hawker, C. J. A renaissance of color: New structures and building blocks for organic electronics. *J. Polym. Sci. Part A Polym. Chem.* **51**, 1263–1271 (2013).
15. Schober, C., Reuter, K. & Oberhofer, H. Virtual Screening for High Carrier Mobility in Organic Semiconductors. *J. Phys. Chem. Lett.* **7**, 3973–3977 (2016).
16. Kunkel, C., Schober, C., Margraf, J. T., Reuter, K. & Oberhofer, H. Finding the Right Bricks for Molecular Legos: A Data Mining Approach to Organic Semiconductor Design. *Chem. Mater.* **31**, 969–978 (2019).
17. Stadler, C., Hansen, S., Kröger, I., Kumpf, C. & Umbach, E. Tuning intermolecular interaction in long-range-ordered submonolayer organic films. *Nat. Phys.* **5**, 153–158 (2009).
18. Iacovita, C. *et al.* Controlling the Dimensionality and Structure of Supramolecular Porphyrin Assemblies by their Functional Substituents: Dimers, Chains, and Close-Packed 2D Assemblies. *Chem. - Eur. J.* **18**, 14610–14613 (2012).
19. Wagner, T., Györök, M., Huber, D., Zeppenfeld, P. & Głowacki, E. D. Quinacridone on Ag(111): Hydrogen bonding versus chirality. *J. Phys. Chem. C* **118**, 10911–10920 (2014).
20. Furukawa, M., Tanaka, H. & Kawai, T. Formation mechanism of low-dimensional superstructure of adenine molecules and its control by chemical modification: A low-temperature scanning tunneling microscopy study. *Surf. Sci.* **445**, 1–10 (2000).
21. Jin, X. *et al.* Pinning-down molecules in their self-assemblies with multiple weak hydrogen bonds of C-H \cdots F and C-H \cdots N. *Chinese Chem. Lett.* **28**, 525–530 (2017).
22. Bouju, X., Mattioli, C., Franc, G., Pujol, A. & Gourdon, A. Bicomponent Supramolecular Architectures at the Vacuum-Solid Interface. *Chem. Rev.* **117**, 1407–1444 (2017).
23. Kim, J. Y. *et al.* Supramolecular interactions of anthraquinone networks on Au(1 1 1): Hydrogen bonds and van der Waals interactions. *Appl. Surf. Sci.* **268**, 432–435 (2013).
24. Yokoyama, T., Yokoyama, S., Kamikado, T., Okuno, Y. & Mashiko, S. Selective assembly on a surface of supramolecular aggregates with controlled size and shape. *Nature* **413**, 619–621 (2001).
25. Wong, K. L. *et al.* Steric blocking as a tool to control molecular film geometry at a metal surface. *Langmuir* **27**, 8735–8737 (2011).
26. Otero, R., Gallego, J. M., De Parga, A. L. V., Martín, N. & Miranda, R. Molecular self-assembly at solid surfaces. *Adv. Mater.* **23**, 5148–5176 (2011).
27. Tan, A. & Zhang, P. Tailoring the growth and electronic structures of organic molecular thin films. *J. Phys. Condens. Matter* **31**, 503001 (2019).
28. Heimel, G. *et al.* Charged and metallic molecular monolayers through surface-induced aromatic stabilization. *Nat. Chem.* **5**, 187–194 (2013).
29. Wang, Q. *et al.* Bilayer Formation vs Molecular Exchange in Organic Heterostructures: Strong Impact of Subtle Changes in Molecular Structure. *J. Phys. Chem. C* **122**, 9480–9490 (2018).
30. Curtis, F. *et al.* GAtor: A First-Principles Genetic Algorithm for Molecular Crystal Structure Prediction. *J. Chem. Theory Comput.* **14**, 2246–2264 (2018).
31. Todorović, M., Gutmann, M. U., Corander, J. & Rinke, P. Bayesian inference of atomistic structure in functional materials. *npj Comput. Mater.* **5**, 35 (2019).
32. Stillinger, F. H. Exponential multiplicity of inherent structures. *Phys. Rev. E* **59**, 48–51 (1999).

33. Maass, F. *et al.* Nonadditivity of the Adsorption Energies of Linear Acenes on Au(111): Molecular Anisotropy and Many-Body Effects. *J. Phys. Chem. Lett.* **10**, 1000–1004 (2019).
34. Packwood, D. M., Han, P. & Hitosugi, T. Chemical and entropic control on the molecular self-assembly process. *Nat. Commun.* **8**, 14463 (2017).
35. Freibert, A., Dieterich, J. M. & Hartke, B. Exploring self-organization of molecular tether molecules on a gold surface by global structure optimization. *J. Comput. Chem.* **40**, 1978–1989 (2019).
36. Hörmann, L., Jeindl, A., Egger, A. T., Scherbela, M. & Hofmann, O. T. SAMPLE: Surface structure search enabled by coarse graining and statistical learning. *Comput. Phys. Commun.* **244**, 143–155 (2019).
37. Wald, A. On the Efficient Design of Statistical Investigations. *Ann. Math. Stat.* **14**, 134–140 (1943).
38. Forker, R., Meissner, M. & Fritz, T. Classification of epitaxy in reciprocal and real space: rigid versus flexible lattices. *Soft Matter* **13**, 1748–1758 (2017).
39. Blum, V. *et al.* Ab initio molecular simulations with numeric atom-centered orbitals. *Comput. Phys. Commun.* **180**, 2175–2196 (2009).
40. Perdew, J. P., Burke, K. & Ernzerhof, M. Generalized Gradient Approximation Made Simple. *Phys. Rev. Lett.* **77**, 3865–3868 (1996).
41. Tkatchenko, A. & Scheffler, M. Accurate Molecular Van Der Waals Interactions from Ground-State Electron Density and Free-Atom Reference Data. *Phys. Rev. Lett.* **102**, 073005 (2009).
42. Ruiz, V. G., Liu, W., Zojer, E., Scheffler, M. & Tkatchenko, A. Density-Functional Theory with Screened van der Waals Interactions for the Modeling of Hybrid Inorganic-Organic Systems. *Phys. Rev. Lett.* **108**, 146103 (2012).
43. Neugebauer, J. & Scheffler, M. Adsorbate-substrate and adsorbate-adsorbate interactions of Na and K adlayers on Al(111). *Phys. Rev. B* **46**, 16067–16080 (1992).
44. Sojka, F., Meissner, M., Zwick, C., Forker, R. & Fritz, T. Determination and correction of distortions and systematic errors in low-energy electron diffraction. *Rev. Sci. Instrum.* **84**, 015111 (2013).
45. Mehler, A. *et al.* Ordered Superstructures of a Molecular Electron Donor on Au(111). *Langmuir* **33**, 6978–6984 (2017).
46. Meissner, M. *et al.* Flexible 2D Crystals of Polycyclic Aromatics Stabilized by Static Distortion Waves. *ACS Nano* **10**, 6474–6483 (2016).
47. Gruenewald, M. *et al.* Impact of a molecular wetting layer on the structural and optical properties of tin(II)-phthalocyanine multilayers on Ag(111). *Phys. Rev. B* **93**, 115418 (2016).

Acknowledgements

We acknowledge fruitful discussions with M. Scherbela and A.T. Egger while refining the methods and interpreting the theoretical results. Funding through the projects of the Austrian Science Fund (FWF): P28631-N30 and Y1175, by the Deutsche Forschungsgemeinschaft (DFG): FR 875/16-1 and FR 875/19-1, and by the Federal Ministry of Education and Research of Germany (BMBF – KMU-NetC, 03VNE1052C) within the project “InspirA” is gratefully acknowledged. Computational results have been achieved in part using the Vienna Scientific Cluster (VSC) and using resources of the Argonne Leadership Computing Facility, which is a DOE Office of Science User Facility supported under Contract DE-AC02-06CH11357.

Author contribution

A.J., L.H., and O.T.H. conceived and developed the theoretical methods used in this manuscript. A.J. carried out all theoretical calculations and analyses. J.D., F.S., T.F., and R.F. conceived the experiments used in this work. J.D. and F.S. carried out the experiments and subsequent analyses. A.J. and O.T.H. wrote the main paper, A.J. and J.D. wrote the Supplementary Information. All authors discussed the results and their implications and commented on the manuscript at all stages.

Competing interests

The authors declare no competing interests.

Supplementary Information to “Explaining the non-intuitive surface self-assembly of acenequinones on Ag(111): More than just LEGO”

A. Jeindl¹, J. Domke², L. Hörmann¹, F. Sojka², R. Forker², T. Fritz², and O.T. Hofmann^{1*}

¹ Institute of Solid State Physics, NAWI Graz, Graz University of Technology, Petersgasse 16, 8010 Graz, Austria

² Institute of Solid State Physics, Friedrich Schiller University Jena, Helmholtzweg 5, 07743 Jena, Germany

*Corresponding author: o.hofmann@tugraz.at

Content

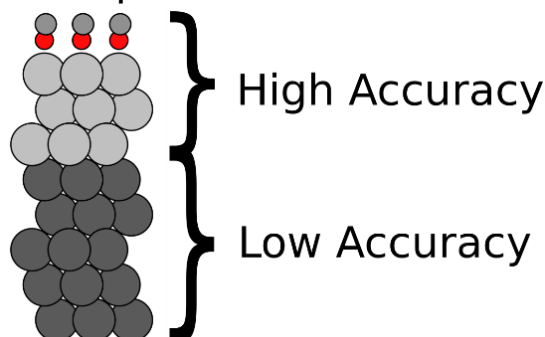
1	Supporting methodology (theory).....	2
1.1	Mixed basis set approach	2
1.2	Hyper parameters used for SAMPLE.....	2
1.3	Finding adsorption geometries	3
1.4	Generating motif candidates.....	3
1.5	Simulating kinematic diffraction.....	3
2	Supplementary methodology (experiment)	4
2.1	Details of the sample preparation.....	4
2.2	Details of the FFT fit procedure	4
3	Predictions of all possible motifs.....	7
4	Unit cell comparison.....	9
5	Additional pair potential plots	10

1 Supporting methodology (theory)

1.1 Mixed basis set approach

A crucial part in surface slab calculations is the convergence of the number of slab layers. There need to be enough layers below the surface to resemble bulk-like behavior, but as little as possible to reduce computational cost. In our case, more than 6 layers of silver are necessary for a sufficiently converged adsorption energy, which increased the computational cost to an intractable level. Fortunately, a fully accurate quantum mechanical description is only necessary for the interaction area of a molecule and the substrate. Thus, the fact that FHI-aims¹⁻⁵ uses atom-centered basis sets was utilized in the following way: The three uppermost layers of the surface slab were calculated with a tight and thoroughly converged basis, while the lower five layers (which are further away from the molecule) were only represented via a very light basis (see Supplementary Fig. 1).

Supplementary Fig. 1: Visualization of CO adsorbed on the mixed basis used in this manuscript.



The light grey layers consist of Ag atoms with tight basis while the dark grey atoms were calculated with a much looser basis.

1.2 Hyper parameters used for SAMPLE

For the SAMPLE approach⁶ several hyper parameters are necessary. All of those hyper parameters were varied systematically to maximize the log likelihood in the Bayesian linear regression formalism. Supplementary Table 1 contains all optimized hyper parameters used for the prediction of the three systems. Decay length differences arise from the different molecule sizes. To avoid the need to fit the highly repulsive Pauli repulsion region with Bayesian linear regression, SAMPLE uses a minimal distance threshold for all atom-species combinations. For this work the following thresholds were used: O \leftrightarrow H: 1.6 Å; O \leftrightarrow O: 2.4 Å, H \leftrightarrow H: 1.6 Å; C \leftrightarrow H: 2.3 Å; C \leftrightarrow O: 2.5 Å.

Supplementary Table 1: Hyper parameters of the SAMPLE approach used for the structure prediction of benzo-, anthra- and pentacenequinone.

Hyper parameter	B2O	A2O	P2O
Adsorption energy uncertainty	100 meV	100 meV	100 meV
Interaction energy uncertainty	300 meV	300 meV	300 meV
DFT data uncertainty	10 meV	5 meV	5 meV
Decay length	5 Å	5 Å	10 Å
Decay power	3	3	3
Decay length feature space	12	9	5
Feature threshold	0.0075	0.0075	0.01

1.3 Finding adsorption geometries

Gaussian process regression⁷ was used to interpolate the adsorption geometries of single molecules on a multidimensional potential energy surface, in the following way: First, an individual molecule was optimized lying flat on the surface (as was also found experimentally for P2O)⁸ at an unspecific in-plane position to estimate the general distortions of the molecule upon adsorption on a surface. This optimized molecule was symmetrized and lifted from the surface by 0.1 Å to reduce the influence of the Pauli repulsion, i.e. to avoid “ramming” the molecule into the substrate. The lateral position of minima is not affected by the slightly larger vertical distance. This approach resulted in a mean distance between the center of the uppermost Ag layer and the molecular backbone of 2.4 Å for B2O, 2.9 Å for A2O and 3.0 Å for P2O. Then, a full potential energy surface (PES) for movement of this molecule along the x-y plane and rotation around the z-axis was mapped by performing approx. 50 DFT calculations. Subsequently, a geometry optimization for the full molecule and substrate was performed from all extrema in the aforementioned PES, allowing the whole molecule to relax until the remaining forces were below a suitable threshold for all atoms (0.02 eV/Å for A2O and P2O, 0.05 eV/Å for B2O). Those adsorption geometries were then symmetrized according to the applicable substrate symmetries to remove geometry-optimization artefacts. All final adsorption geometries, where at least one atom position differed by more than 0.1 Å (with symmetries taken into account), were considered as separate adsorption geometries.

1.4 Generating motif candidates

For all three molecules in this study we varied the number of molecules per cell N_A from 1 to 4 and varied the unit cell size from $N_A * A_{min}$ to $N_A * (A_{min} + 5)$ to ensure that experimentally feasible configurations are part of the prediction set. Here A_{min} is the minimal cell size where configurations could be built without interfering with minimal distance thresholds set in SAMPLE.

For B2O and A2O we additionally constructed tightly packed polymorphs with up to 6 molecules per unit cell. The hexagonal cell for A2O was found by constructing all configurations for hexagonal unit cells with six molecules per unit cell up to 90 surface atoms per cell.

1.5 Simulating kinematic diffraction

To compare the theoretical structure to LEED results, simulations based on kinematic diffraction theory were performed. Therefore, the location and intensity of the peaks were calculated as the square of the structure factors $n_{\vec{G}} = \sum_{atoms} f_{atom}(\vec{G}) \exp(-i\vec{G}\vec{r}_{atom})$. Here \vec{G} are the reciprocal lattice vectors of the crystal and \vec{r}_{atom} the positions of atoms in the unit cell, respectively. The atomic form factors were each approximated with $f_{atom}(G) = \sum_{i=1}^n a_i \exp\left(-b_i \left(\frac{G}{4\pi}\right)^2\right)$ where a_i and b_i were taken from the international tables for crystallography(2006).⁹

2 Supplementary methodology (experiment)

2.1 Details of the sample preparation

The experimental monolayers for B2O (CAS: 106-51-4, nominal purity 99.5%), A2O (CAS: 84-65-1, nominal purity 97%) and P2O (CAS: 3029-32-1, nominal purity 99%) were deposited at room temperature (296 K) in an ultra-high vacuum chamber with a base pressure better than $5 \cdot 10^{-10}$ mbar via physical vapor deposition on clean Ag(111) single crystals. The single crystals were obtained from MaTeck GmbH and cleaned by Ar^+ sputtering at 700 eV and incident angles of $\pm 45^\circ$ to the surface normal, followed by annealing at 800 K. Sputtering and annealing were cyclically repeated until the surface quality was satisfactory, as confirmed by low energy electron diffraction (LEED).

Only A2O and P2O could be further purified by temperature gradient vacuum sublimation using a CreaPhys DSU-05. B2O was purified in a home-built sublimation device consisting of two separate glass tubes, dubbed reservoir and sublimation tube, which are connected to each other by an angle valve, with the sublimation tube additionally attached to the deposition chamber by a dosing valve. B2O was initially filled into the reservoir tube and evacuated with both valves open. The reservoir tube was subsequently heated by a stream of hot air until a sufficient amount of B2O deposited on the walls of the sublimation tube, after which both valves were closed.

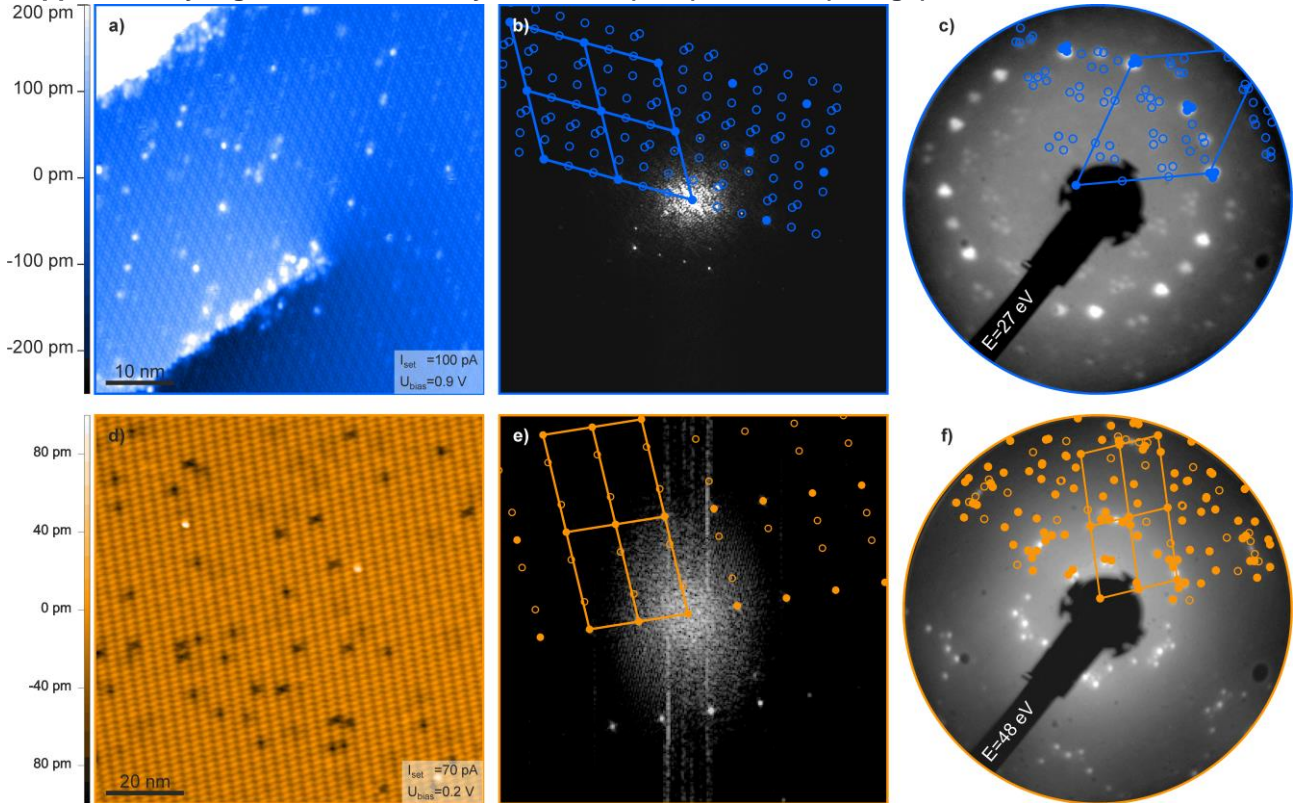
Monolayer deposition on Ag(111) for B2O was carried out by positioning the sample in approximately 30 cm distance and in direct line of sight to the dosing valve and opening it until the chamber pressure reached $1 \cdot 10^{-6}$ mbar, after which the valve was kept open for 10 minutes. The purified A2O was filled into another glass tube and connected to the deposition chamber via a dosing valve. During layer deposition the sample was placed in approximately 30 cm distance and in direct line of sight to the dosing valve, and the dosing valve was opened for 15 minutes. P2O was deposited by thermal evaporation from a shutter-controlled effusion cell held at 450 K with a deposition time of 10 minutes.

2.2 Details of the FFT fit procedure

Since the LEED device used by us typically probes a surface area in the order of 1 mm^2 , the resulting images usually show a superposition of all motifs present in that area, e.g., symmetrically equivalent domains and other polymorphs, if present. For this reason, we additionally performed a detailed analysis of the STM images to ensure the assignment of the epitaxial relations determined by LEED to the motifs presented in STM as well as to increase the accuracy. We found motifs exhibiting Moiré patterns in their respective STM images on all samples presented in this study. These patterns show up as discrete spots in the two-dimensional Fourier transforms (FFT) as well, and their spot positions can be described in the same way as multiple scattering in geometric scattering theory, thus enabling an analysis¹⁰ with LEEDLab¹¹. For that purpose, we subjected the STM images showing a single domain of the motif under investigation, featuring molecular resolution as well as a Moiré pattern, to an FFT. We then determined the epitaxial relation by fitting the respective reciprocal lattice including the Moiré spots to the FFT, optimizing the adsorbate lattice and substrate lattice simultaneously, thus circumventing the distortions typically present in STM. This procedure yielded the epitaxy matrices for B2O and P2O directly (see Supplementary Fig. 2). However, it is not applicable to the hexagonal A2O structure, where we observed no Moiré patterns (likely due to its commensurate registry). Instead, we analyzed an STM image containing the motif presented in the main text (Motif A) and an additional, non-commensurate motif (Motif B), which shows a Moiré contrast, as can be seen in Supplementary Fig. 3. By taking a detail of the STM image containing only Motif B, we determined its lattice vectors relative to the substrate vectors, which then contain the local distortion, using the

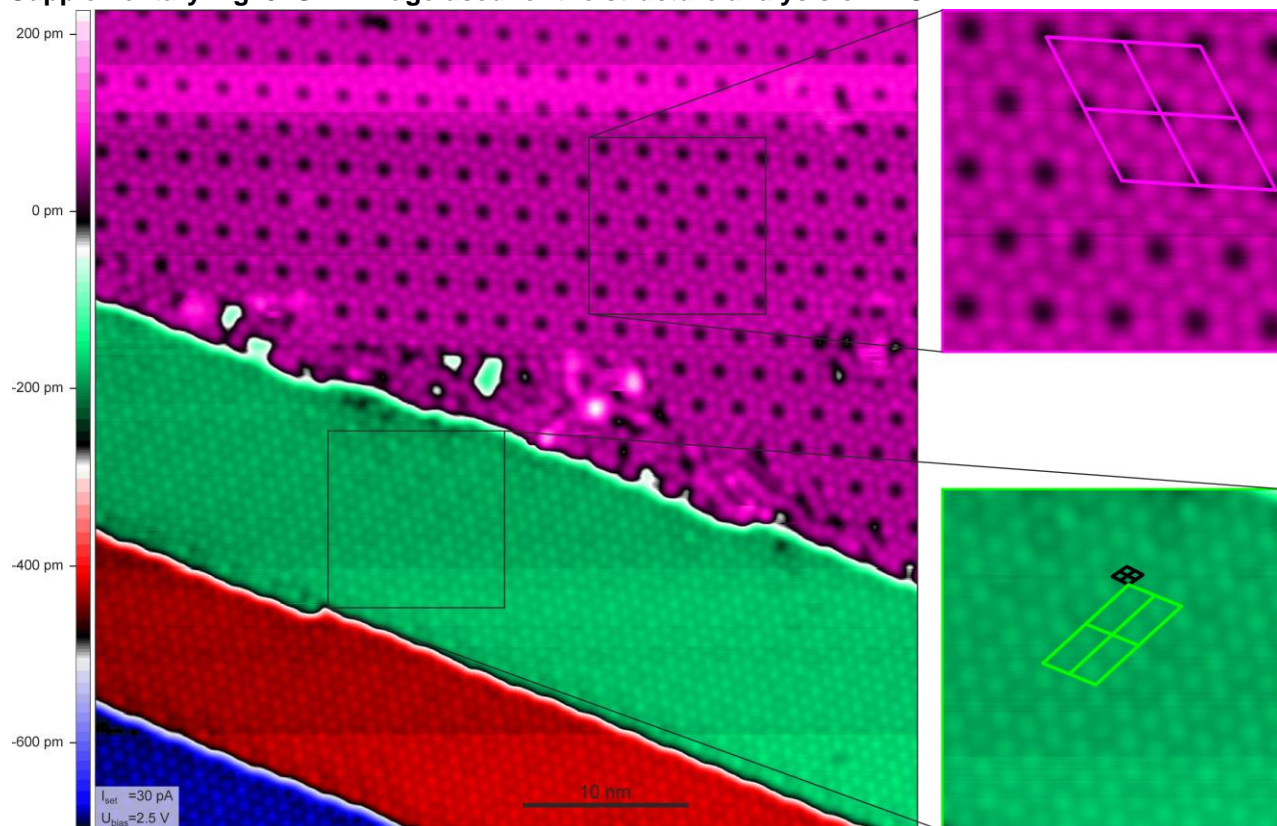
procedure described earlier. We presume the distortions to be constant for the image as a whole and therefore particularly for a detail containing only Motif A and use this detail to determine the lattice vectors of Motif A relative to Motif B, this time solely optimizing the adsorbate lattice. We then calculated the epitaxial relation of Motif A relative to the substrate by combining the two derived epitaxy matrices via matrix multiplication. By comparing both obtained motifs in reciprocal space to the LEED image of the A2O sample (Supplementary Fig. 4), it is evident that a structure determination based on LEED alone would remain ambiguous due to the similarity in many spot positions. Motif B is likely a kinetically trapped structure and could thus, and due to its non-commensurate nature, not be found within the theoretical framework (For details see Supplementary Section 3.1).

Supplementary Fig. 2: Structure analysis of B2O (blue) and P2O (orange)



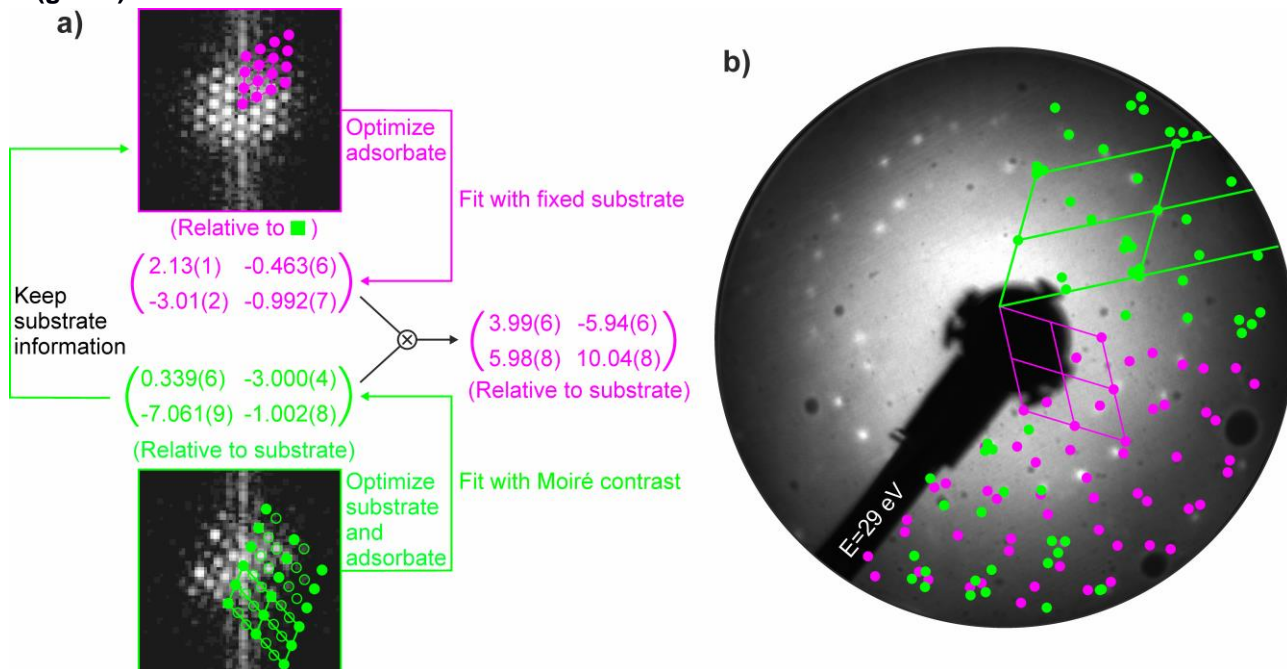
STM images of B2O (a) and P2O (d) (same sample as the images in Fig. 4) b,e, FFTs of (a) and (d), respectively, superimposed with the fitted reciprocal lattice. Several lattice points (dots) as well as Moiré frequencies (circles) are highlighted. c,f, LEED images (same measurement as Fig. 4) at a given primary electron energy E superimposed with a simulation of the reciprocal lattice (dots) including multiple scattering (circles) and symmetrically equivalent domains as fitted to (b) and (e), respectively.

Supplementary Fig. 3: STM image used for the structure analysis of A2O



Details of Motif A (top, magenta color code) and Motif B (bottom, green color code) feature representations of the unit cells of the motifs fitted to an FFT of the respective detail. The substrate lattice characterizing the distortions present in the image as determined by the fit is shown in comparison to Motif B (black lattice cell).

Supplementary Fig. 4: Reciprocal space representation of the lattices of Motif A (magenta) and Motif B (green)



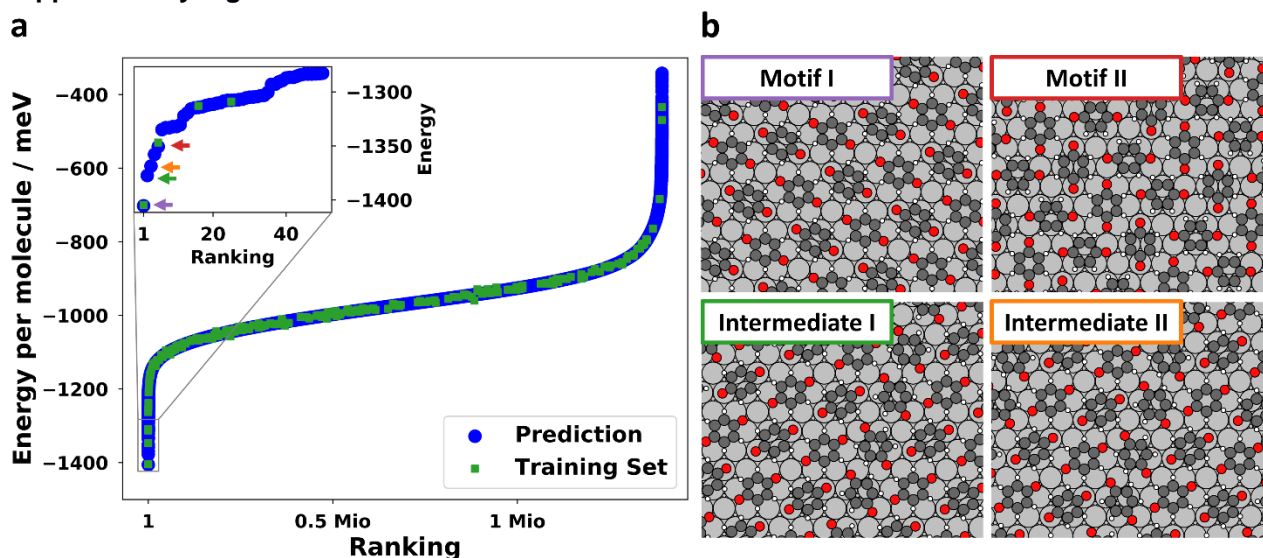
a, FFTs of the details displayed in Supplementary Fig. 3 superimposed with the reciprocal unit cell as fitted to the FFT including the respective epitaxy matrix. Several reciprocal lattice points (filled circles) as well as Moiré spots (open circles) for Motif A and B are displayed as guide to the eye. **b**, LEED of the sample measured at 296 K, superimposed with a simulation of the reciprocal lattice points including symmetrically equivalent lattice representations.

3 Predictions of all possible motifs

To obtain the motifs discussed in the main paper, first all possible motifs within the model discretization were created (see Supplementary Section 1.4) to then predict all their energies. The energy models used for prediction were trained on a representative number of D-optimally chosen calculations (249 for B₂O, 245 for A₂O and 84 for P₂O). To speed up training, intermolecular interaction data obtained from free-standing monolayers (i.e., removed substrate) was used as prior for the on-surface models. The prediction results and representative, energetically favorable motifs are presented in Supplementary Figures 5 to 7.

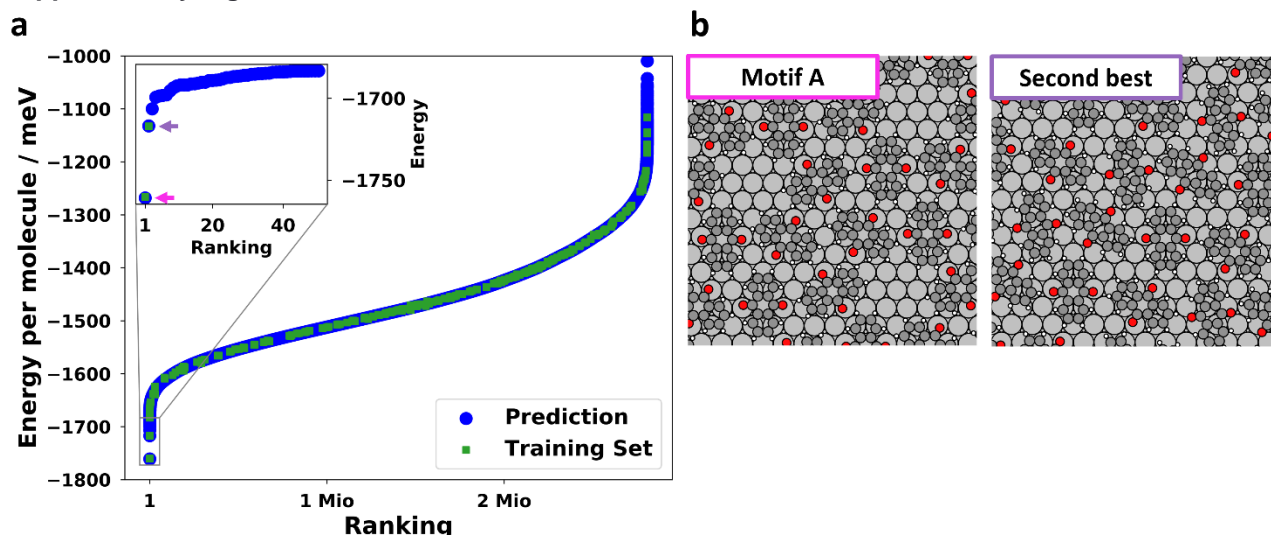
The reliability of the model was verified via leave-one-out cross validation (LOOCV) uncertainties of 11 meV for B₂O, 9 meV for A₂O and 20 meV for P₂O. The LOOCV uncertainty is obtained by calculating the root mean square error for all data points, but instead of using a separate test set, the deviation for each data point is obtained by training on all points but the one for which the deviation is probed. This, to some extent, is a worst-case measure of the uncertainty, as, if there are important data points in the set, the uncertainty for those will be very large, increasing the overall uncertainty. Due to the fact that our points are chosen D-optimally, meaning that the most important points should be calculated, we consider the LOOCV uncertainty superior to simple RMSE evaluation on a separate test set, additionally saving the costs of calculating an expensive test set.

Supplementary Fig. 5: Prediction and best theoretical motifs for B₂O



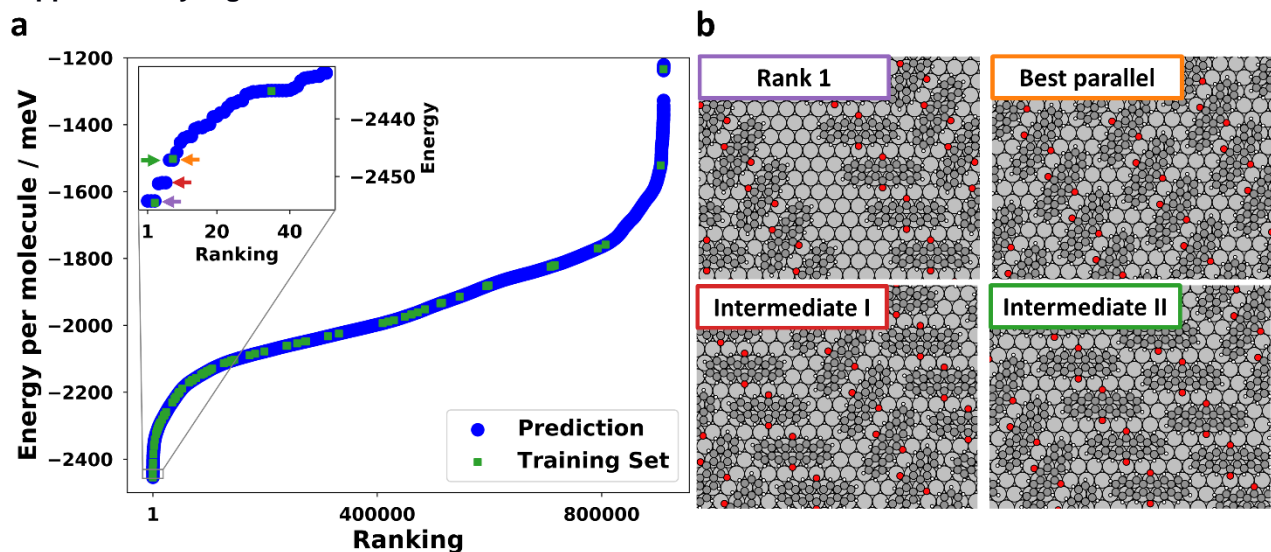
a, Visualization of the formation energies per molecule for all predicted polymorphs of B₂O and ranking according to energy from most favorable to least favorable. Points used for the training of the respective models are visualized with green rectangles. **b**, Motifs which were used for comparison to experiment and two intermediate motifs that rank between them.

Supplementary Fig. 6: Prediction and best theoretical motifs for A2O



a, Visualization of the formation energies per molecule for all predicted polymorphs of A2O and ranking according to energy from most favorable to least favorable. Points used for the training of the respective models are visualized with green rectangles. **b**, Best motif (corresponding Motif A in Supplementary Fig. 3) and second-best motif. Predictions of Motif B of Supplementary Section 2.3 are beyond our theoretical framework due to its point-on-line epitaxy.

Supplementary Fig. 7: Prediction and best theoretical motifs for P2O



a, Visualization of the formation energies per molecule for all predicted polymorphs of P2O and ranking according to energy from most favorable to least favorable. Points used for the training of the respective models are visualized with green rectangles. **b**, Visualization of the motifs that are predicted energetically slightly more beneficial (< 20 meV) than the experimental motif (Best parallel).

4 Unit cell comparison

Table 1 shows the most important unit cells presented in Fig. 4, a thorough analysis of all presented unit cells and uncertainties of the epitaxy matrices is given in Supplementary Table 2. A graphical representation of the unit cell parameters used for Table 1 and Supplementary Table 2 is presented in Supplementary Fig. 9. For the calculation of the lattice vector lengths in Supplementary Table 2 we used the converged lattice constant of our calculations, which amounts to 4.019 Å for the conventional unit cell (corresponding to a minimal Ag-Ag distance of 2.842 Å).

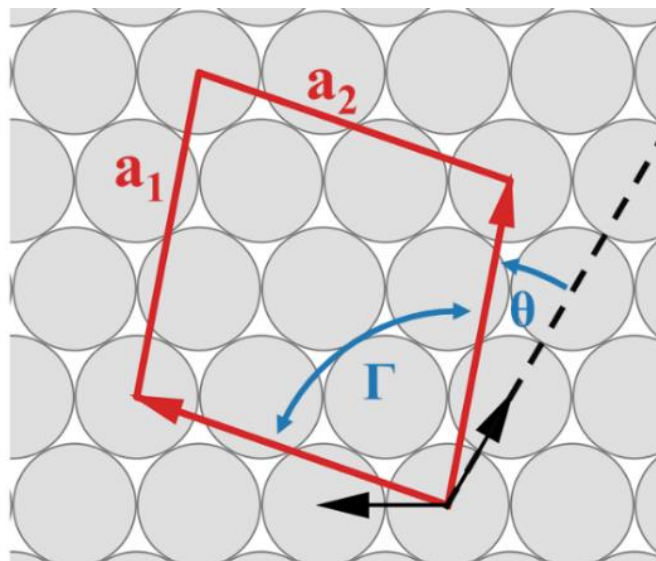
The experimental uncertainties of the matrix elements indicate the simple standard deviations of the values, while each value represents the result of a directly optimized parameter of the fit routine used. Only the matrix elements for A2O are derived by the combination of two different matrices (as shown in Supplementary Fig. 4). Therefor the uncertainties of this matrix are obtained via Gaussian error propagation as well as the uncertainties of the lattice parameters.

Supplementary Table 2: Comparison of experimental (grey background) and theoretical unit cells.

a_1 , a_2 : Lengths of lattice vectors derived from the epitaxy matrices in combination with the theoretical substrate lattice vectors; Γ : angle of the unit cell; Θ : angle between a_1 and the primitive substrate axis. Experimental uncertainties are indicated with brackets.

		a_1 [Å]	a_2 [Å]	Γ [°]	Θ [°]	A [Å ²]	Epitaxy
B2O small	I	6.875(5)	6.603(3)	119.88(5)	-14.28(2)	39.36(4)	$\begin{pmatrix} 2.000(1) & -0.689(1) \\ 0.667(1) & 2.584(1) \end{pmatrix}$
		6.512	6.512	98.21	10.89	41.97	$\begin{pmatrix} 2.5 & 0.5 \\ 0.5 & 2.5 \end{pmatrix}$
B2O large (Motif I)	I	11.926(8)	13.21(1)	91.21(8)	14.40(5)	157.5(2)	$\begin{pmatrix} 4.667(2) & 1.205(3) \\ 1.334(2) & 5.169(3) \end{pmatrix}$
		13.024	13.024	98.21	10.89	167.87	$\begin{pmatrix} 5 & 1 \\ 1 & 5 \end{pmatrix}$
B2O small	II	6.875(5)	6.603(3)	119.88(5)	-14.28(2)	39.36(4)	$\begin{pmatrix} 2.000(1) & -0.689(1) \\ 0.667(1) & 2.584(1) \end{pmatrix}$
		6.512	7.211	121.07	-10.89	40.22	$\begin{pmatrix} 2 & -0.5 \\ 0.5 & 2.75 \end{pmatrix}$
B2O large (Motif II)	II	13.75(1)	11.448(6)	88.51(7)	-14.30(3)	157.4(2)	$\begin{pmatrix} 4.000(3) & -1.380(2) \\ 3.334(2) & 4.476(2) \end{pmatrix}$
		13.024	12.388	94.31	-10.89	160.88	$\begin{pmatrix} 4 & -1 \\ 3 & 5 \end{pmatrix}$
A2O		24.6(3)	24.9(2)	120(1)	-36.5(4)	530(10)	$\begin{pmatrix} 3.99(6) & -5.94(6) \\ 5.98(8) & 10.04(8) \end{pmatrix}$
		24.776	24.776	120.00	-36.57	531.60	$\begin{pmatrix} 4 & -6 \\ 6 & 10 \end{pmatrix}$
P2O		14.96(2)	8.156(4)	95.92(8)	40.78(3)	121.3(2)	$\begin{pmatrix} 2.000(1) & -3.969(6) \\ 3.000(1) & 2.719(2) \end{pmatrix}$
		15.038	8.526	100.89	40.89	125.90	$\begin{pmatrix} 2 & -4 \\ 3 & 3 \end{pmatrix}$

Supplementary Fig. 9: Visual explanation of the unit cell parameters used for cell comparison

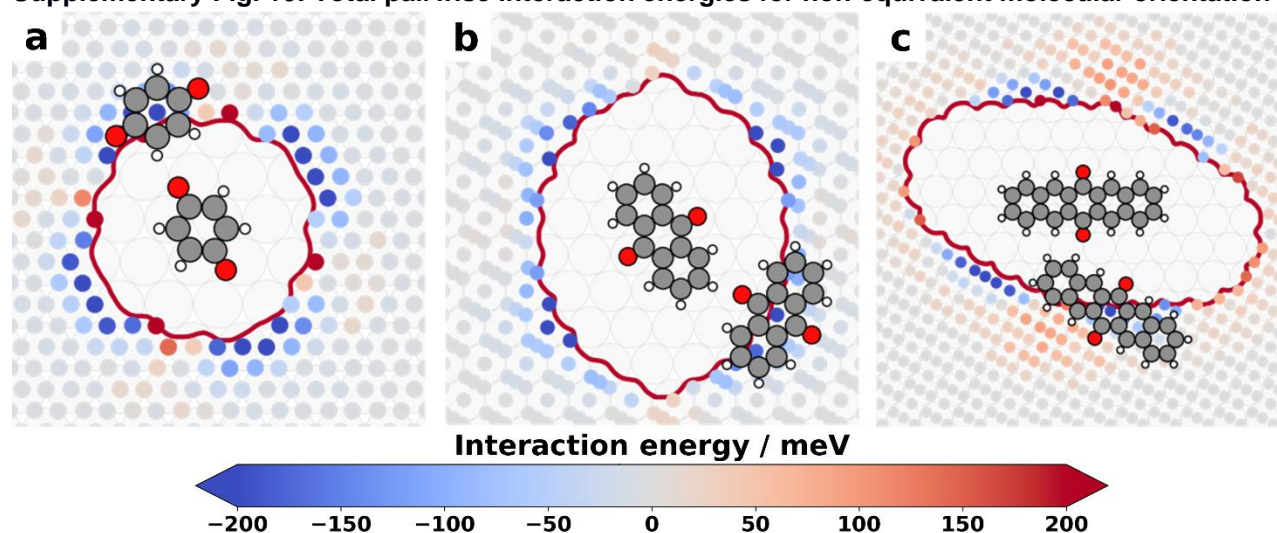


a_1 and a_2 are the lengths of the unit cell lattice; Γ is defined as the enclosing angle of the unit cell vectors; Θ represents the angle between the first lattice vector and a primitive substrate axis, negative values correspond to angles in anticlockwise direction.

5 Additional pair potential plots

Figure 3 visualized interactions of pairs of molecules with parallel alignment. Supplementary Fig. 10 presents a selection of interaction maps for pairs with non-equal orientation.

Supplementary Fig. 10: Total pairwise interaction energies for non-equivalent molecular orientation



Each circle represents a possible pairwise interaction between the central molecule and an adjacent molecule centered at the circle position for (a) B₂O, (b) A₂O and (c) P₂O. The red contour shows the minimal distance before a pair is considered colliding. The circle color indicates the corresponding interaction energy.

References

1. Blum, V. *et al.* Ab initio molecular simulations with numeric atom-centered orbitals. *Comput. Phys. Commun.* **180**, 2175–2196 (2009).
2. Havu, V., Blum, V., Havu, P. & Scheffler, M. Efficient $O(N)$ integration for all-electron electronic structure calculation using numeric basis functions. *J. Comput. Phys.* **228**, 8367–8379 (2009).
3. Marek, A. *et al.* The ELPA library: scalable parallel eigenvalue solutions for electronic structure theory and computational science. *J. Phys. Condens. Matter* **26**, 213201 (2014).
4. Ihrig, A. C. *et al.* Accurate localized resolution of identity approach for linear-scaling hybrid density functionals and for many-body perturbation theory. *New J. Phys.* **17**, 093020 (2015).
5. Yu, V. W. *et al.* ELSI: A unified software interface for Kohn–Sham electronic structure solvers. *Comput. Phys. Commun.* **222**, 267–285 (2018).
6. Hörmann, L., Jeindl, A., Egger, A. T., Scherbela, M. & Hofmann, O. T. SAMPLE: Surface structure search enabled by coarse graining and statistical learning. *Comput. Phys. Commun.* **244**, 143–155 (2019).
7. Todorović, M., Gutmann, M. U., Corander, J. & Rinke, P. Bayesian inference of atomistic structure in functional materials. *npj Comput. Mater.* **5**, 35 (2019).
8. Heimel, G. *et al.* Charged and metallic molecular monolayers through surface-induced aromatic stabilization. *Nat. Chem.* **5**, 187–194 (2013).
9. Colliex, C. *et al.* Electron diffraction. in *International Tables for Crystallography* 259–429 (International Union of Crystallography, 2006). doi:10.1107/97809553602060000593
10. Gruenewald, M. *et al.* Impact of a molecular wetting layer on the structural and optical properties of tin(II)-phthalocyanine multilayers on Ag(111). *Phys. Rev. B* **93**, 115418 (2016).
11. Sojka, F., Meissner, M., Zwick, C., Forker, R. & Fritz, T. Determination and correction of distortions and systematic errors in low-energy electron diffraction. *Rev. Sci. Instrum.* **84**, 015111 (2013).